Long-range order in a three-dimensional random-tiling quasicrystal

Laurence J. Shaw, Veit Elser, and Christopher L. Henley
Department of Physics, Cornell University, Ithaca, New York 14853-2501
(Received 5 July 1990)

Monte Carlo simulations are performed on the rhombohedral random-tiling model of icosahedral quasicrystals. Long-range order is observed in agreement with a squared-gradient form of the coarse-grained free energy, and the two independent phason elastic constants are determined. Schematic transmission electron micrographs, generated by two-dimensional projections of the tile vertices of a typical random configuration, display phason disorder only for sufficiently thin samples.

I. INTRODUCTION

Recently, quasicrystals with resolution-limited Bragg diffraction peaks were discovered in the family *i*(Al-Cu-Fe)–*i*(Al-Cu-Ru).[1–3] Among the explanations of quasicrystal ordering, only two predict long-range order in the sense of Bragg peaks in three dimensions: (1) the perfectly quasiperiodic model, where *energetic* considerations (such as matching rules) enforce a ground state analogous to a perfect crystal;[4–5] (2) the equilibrium random-tiling model, according to which there are many nearly degenerate ways of packing structural units, so that a phase with maximum *entropy* is selected.[7–9] In model (2) the phason degrees of freedom which express fluctuations around an average icosahedral symmetry are expected to have the simple form of gradient-squared elasticity (when suitably coarse grained);[10,11] this leads to Bragg peaks in three dimensions and, in contrast to model (1), diffuse scattering due to the phason fluctuations.

The random-tiling explanation furthermore predicts that, since different packings are not exactly degenerate, the quasicrystal phase will probably transform upon cooling to a crystal.[12,9] Of course, it is also possible that the low-temperature phase is an energetically stabilized *quasi*crystal. However, this possibility defeats the main appeal of the random-tiling model: in real materials it is easier to envision structural energetics which favor the near degeneracy required by random tiling than the absolute minimum of energy required by the quasiperiodic model. We note that the only known equilibrium quasicrystal Al-Cu-Fe transforms at low temperatures to a crystal.[13,3] However, at the same time, high-resolution transmission electron microscopy (HRTEM) images of *i*(Al-Cu-Fe) display no visible deviations from perfect quasiperiodicity:[14] rows of spots are separated by a Fibonacci sequence of long and short spacings.

Numerical work on two-dimensional random-tiling models, including Monte Carlo simulations,[15,16] exact transfer-matrix calculations,[17] and transfer-matrix Monte Carlo calculations,[18] supports the squared-gradient free-energy theory and the resulting predictions of an entropically favored state with five-fold symmetry and quasi-long-range order. Recently Tang's Monte Carlo simulation of a random tiling of Ammann rhombohedra has produced the first numerical confirmation of long-range order in three dimensions.[19] Tang generated and analyzed a diffraction pattern of the equilibrated tiling, confirmed the existence of long-range order, and determined the values of the phason elastic constants. Another Monte Carlo study by Strandburg finds the entropy to be 0.23 per vertex.[20]

Here we report the results of a simulation similar to Tang's, but (1) we determine the elastic constants by a different, more accurate method; (2) we investigate the dynamics of the model in more detail; and (3) we project tile vertices within slices onto a plane to produce schematic HRTEM images. We find that as slab thickness increases, the apparent density of defects in rows of spots decreases. An analytic argument shows that this occurs generally in any random-tiling model, and so we would predict defect-free HRTEM images for sufficiently thick specimens. In our system, images from slices with a thickness of 25 rhombohedral edge lengths already show few defects.

In Sec. II we introduce our notation, review the relevant continuum theory of phason fluctuations, and present the theory of the Monte Carlo dynamics. Section III outlines the details of the simulation. Results and conclusions are presented in Sec. IV.

II. THEORY

A. Notation

In the three-dimensional icosahedral tiling there are two types of rhombohedra. The prolate rhombohedron has corner spherical angles of $\pi/5$ and $3\pi/5$ and the oblate rhombohedron has corner spherical angles of $\pi/5$ and $7\pi/5$. The faces of the rhombohedra are identical rhombi with acute angle $\cos^{-1}(1/\sqrt{5})$.

A particular tiling may be viewed as the projection of a connected three-dimensional surface embedded in a six-dimension simple-cubic lattice. Each vertex of the tiling is specified by a vector

$$\mathbf{r}^{\parallel} = \sum_{\alpha=1}^{6} n_\alpha \mathbf{e}_\alpha^{\parallel} , \tag{1}$$

where n_α are integers and $\mathbf{e}_\alpha^\parallel$ are projections onto the three-dimensional "physical space" of the basis vectors of the six-dimensional simple-cubic lattice. The corresponding "phason" coordinate of the vertex is

$$\mathbf{r}^\perp = \sum_{\alpha=1}^{6} n_\alpha \mathbf{e}_\alpha^\perp \tag{2}$$

and the six-dimensional position is

$$\mathbf{r}^\parallel + \mathbf{r}^\perp = \sum_{\alpha=1}^{6} n_\alpha (\mathbf{e}_\alpha^\parallel + \mathbf{e}_\alpha^\perp) = \sum_{\alpha=1}^{6} n_\alpha \mathbf{e}_\alpha \ . \tag{3}$$

Following the conventions of Jarić,[11]

$$\begin{aligned} &\mathbf{e}_1^\parallel = \eta(\tau,0,1), \quad \mathbf{e}_2^\parallel = \eta(\tau,0,-1), \\ &\mathbf{e}_3^\parallel = \eta(1,\tau,0), \quad \mathbf{e}_4^\parallel = \eta(0,1,\tau) \ , \\ &\mathbf{e}_5^\parallel = \eta(0,-1,\tau), \quad \mathbf{e}_6^\parallel = \eta(1,-\tau,0) \ , \end{aligned} \tag{4}$$

and

$$\begin{aligned} &\mathbf{e}_1^\perp = \eta(1,0,-\tau), \quad \mathbf{e}_2^\perp = \eta(1,0,\tau), \\ &\mathbf{e}_3^\perp = \eta(-\tau,1,0), \quad \mathbf{e}_4^\perp = \eta(0,-\tau,1) \ , \\ &\mathbf{e}_5^\perp = \eta(0,\tau,1), \quad \mathbf{e}_6^\perp = \eta(-\tau,-1,0) \ , \end{aligned} \tag{5}$$

where $\eta \equiv (2+\tau)^{-1/2}$ and $\tau \equiv \frac{1}{2}(1+\sqrt{5})$.

The long-wavelength behavior of the interface is described by the coarse-grained phason coordinate

$$\mathbf{h}(\mathbf{r}^\parallel) = \langle \mathbf{r}^\perp \rangle_{\mathbf{r}^\parallel} \ , \tag{6}$$

where $\langle \cdots \rangle_{\mathbf{r}^\parallel}$ signifies averaging in the vicinity of $\mathbf{r}^\parallel$ over a region large in comparison with the tile size. (Henceforth we abbreviate $\mathbf{r}^\parallel$ as $\mathbf{r}$.) The phason strain tensor is given by

$$\mathbf{E}(\mathbf{r}) \equiv \nabla_\mathbf{r} \mathbf{h}(\mathbf{r}) \ . \tag{7}$$

"Perfect" quasiperiodic tilings (for which $\mathbf{E}=\mathbf{0}$) consist of the physical-space coordinates of all six-dimensional simple-cubic vertices whose corresponding phason coordinates $\mathbf{r}^\perp$ lie within an "acceptable domain." The acceptance domain is

$$\left\{ \sum_{\alpha=1}^{6} x_\alpha \mathbf{e}_\alpha^\perp : \ 0 < x_\alpha < 1 \right\} , \tag{8}$$

i.e., a projection of the six-dimensional unit cube onto the phason space.[21,22] This domain is the interior of the icosahedrally symmetric rhombic triacontahedron with edge vectors $\mathbf{e}_\alpha^\perp$, $\alpha=1,\ldots,6$. We recall that the projection of the six-dimensional simple-cubic lattice onto the phason space is incommensurate, and so $\sum_\alpha n_\alpha \mathbf{e}_\alpha^\perp \neq \mathbf{0}$ for nonzero integer values of n_α.

1. Periodic tilings

Periodic tilings are produced[23] by commensurate projections. Technically, this means that while using the same physical space basis [Eq. (4)], we replace Eq. (5) by basis vectors $\bar{\mathbf{e}}_\alpha^\perp$, $\alpha=1,\ldots,6$, obtained from the $\mathbf{e}_\alpha^\perp$ of Eq. (5) when τ is replaced by $\bar{\tau}=q/r$, a ratio of integers. Accordingly, the $\mathbf{e}^\perp$ vectors become integrally dependent:

$$\begin{aligned} &q(\bar{\mathbf{e}}_1^\perp + \bar{\mathbf{e}}_2^\perp) + r(\bar{\mathbf{e}}_3^\perp + \bar{\mathbf{e}}_6^\perp) = \mathbf{0} \ , \\ &q(\bar{\mathbf{e}}_3^\perp - \bar{\mathbf{e}}_6^\perp) + r(\bar{\mathbf{e}}_4^\perp - \bar{\mathbf{e}}_5^\perp) = \mathbf{0} \ , \\ &q(\bar{\mathbf{e}}_4^\perp + \bar{\mathbf{e}}_5^\perp) + r(\bar{\mathbf{e}}_1^\perp - \bar{\mathbf{e}}_2^\perp) = \mathbf{0} \ . \end{aligned} \tag{9}$$

We also replace Eq. (2) by

$$\bar{\mathbf{r}}^\perp \equiv \sum_\alpha n_\alpha \bar{\mathbf{e}}_\alpha^\perp \ . \tag{10}$$

The commensurate tiling is then generated using vertices whose commensurate coordinates $\bar{\mathbf{r}}^\perp$ lie within an acceptance domain described by Eq. (8) with $\mathbf{e}_\alpha^\perp \to \bar{\mathbf{e}}_\alpha^\perp$, a rhombic triacontahedron (slightly distorted from icosahedral symmetry) with edge vectors $\bar{\mathbf{e}}_\alpha^\perp$.

The tiling vertices in physical space are still given by Eq. (1), with undistorted basis vectors [Eq. (4)]. Now displacements in the physical space, corresponding to those in Eqs. (9) are

$$\begin{aligned} &q(\mathbf{e}_1^\parallel + \mathbf{e}_2^\parallel) + r(\mathbf{e}_3^\parallel + \mathbf{e}_6^\parallel) = 2\eta(q\tau + r)\hat{\mathbf{x}} \ , \\ &q(\mathbf{e}_3^\parallel - \mathbf{e}_6^\parallel) + r(\mathbf{e}_4^\parallel - \mathbf{e}_5^\parallel) = 2\eta(q\tau + r)\hat{\mathbf{y}} \ , \\ &q(\mathbf{e}_4^\parallel + \mathbf{e}_5^\parallel) + r(\mathbf{e}_1^\parallel - \mathbf{e}_2^\parallel) = 2\eta(q\tau + r)\hat{\mathbf{z}} \ . \end{aligned} \tag{11}$$

If we step from any vertex by one of the vectors in Eqs. (11), then by Eqs. (9) there is no difference in the phason coordinate and consequently the new vertex is also within the acceptance domain, and included in the tiling. Hence, these structures are periodic and Eqs. (11) are vectors in the Bravais lattice. Equations (11) imply that the approximants in this class have cubic symmetry with edge length

$$L = 2\eta(q\tau + r) \ . \tag{12}$$

There is a unique solution in integers of $L^3 = N_P V_P + N_O V_O$ where $V_P = 2\tau^2\eta^3$ and $V_O = 2\tau\eta^3$ are the prolate and oblate tile volumes, respectively. From this the number of tiles (or equivalently, of vertices) in the volume L^3 is easily determined to be $N = N_P + N_O = 4[2q^3 + 3(q+r)qr]$. If q and r are consecutive Fibonacci numbers F_n and F_{n-1} ($F_{n+2} = F_{n+1} + F_n$, for $n \geq 0$, with $F_0 = 0$ and $F_1 = 1$; $F_2 = 1$, $F_3 = 2, \ldots$) so that $\bar{\tau} = q/r = F_n/F_{n-1}$, then these approximants are optimal, in the sense of having the smallest possible phason strain for a given number of tiles. In this case the nonzero components of the phason strain E_n have the values

$$E_n = \frac{\eta}{L}(F_n - F_{n-1}\tau) \sim -\left[\frac{-1}{\tau^2}\right]^n \quad \text{as } n \to \infty \ . \tag{13}$$

A general random-tiling configuration with the desired periodicity can be obtained from the initial structure by a sequence of tile rearrangements (see below). By making the approximant sufficiently large the unavoidable uniform strain [Eq. (13)] is negligible in comparison to the random-phason fluctuations produced by the tile rearrangements.

2. *Elasticity theory, expectation values, correlation functions*

We expect that long-wavelength phasons have the same form of free energy as capillary waves:[24,25]

$$F/kT=\tfrac{1}{2}\int_V \nabla\mathbf{h}(\mathbf{r})\cdot\mathbf{K}\cdot\nabla\mathbf{h}(\mathbf{r})d^3r \ , \tag{14}$$

where $\mathbf{K}$ is the stiffness tensor and V is the system volume. The corresponding form of the free energy in Fourier space is

$$F/kT=\tfrac{1}{2}\sum_{\mathbf{p}} \mathbf{h}(-\mathbf{p})\cdot\mathbf{K}(\mathbf{p})\cdot\mathbf{h}(\mathbf{p}) \ , \tag{15}$$

where

$$\mathbf{h}(\mathbf{p})=\frac{1}{\sqrt{V}}\int_V \mathbf{h}(\mathbf{r})e^{i\mathbf{p}\cdot\mathbf{r}}d^3r \ . \tag{16}$$

It follows from group-theoretic arguments[26,11,27] that in the basis defined by Eqs. (4) and (5)

$$K_{ij}(\mathbf{p})=K_1|\mathbf{p}|^2\delta_{ij} -K_2[(\tfrac{1}{3}|\mathbf{p}|^2+2p_i^2+p_{i+1}^2/\tau-\tau p_{i-1}^2)\delta_{ij}-2p_ip_j] \ , \tag{17}$$

where K_1 and K_2 are independent stiffness constants. Here and henceforth, we understand the subscripts for three-vector components are defined modulo 3. Note that Eq. (17) is invariant under cyclic permutations (123) or to sign changes in any component, when applied to components both in physical and phason space.

The equilibrium expectation value of a quantity X is given by

$$\langle X\rangle=\frac{\sum Xe^{-F/kT}}{\sum e^{-F/kT}} \ , \tag{18}$$

where the summation is over tiling configurations. We will make particular use of wave vectors along one of the coordinate axes, defining $\mathbf{p}_l$ as the wave vector whose only nonzero component is $(\mathbf{p}_l)_l=p$, for $l=1,2,3$ (defined modulo 3). For such a wave vector, the stiffness tensor $\mathbf{K}(\mathbf{p})$ is diagonal (in Jarić's basis). Thus by Eqs. (15) and (17) the equal-time expectation value $\langle h_i(\mathbf{p}_j)h_k^*(\mathbf{p}_l)\rangle$ is nonzero only when $i=k$ and $\mathbf{p}_j=\mathbf{p}_l$, and

$$\langle|h_i(\mathbf{p}_j)|^2\rangle=\frac{1}{K_{ii}(\mathbf{p}_j)} \ . \tag{19}$$

The linear-response dynamics can always be described by an equation of the form

$$dh_i(\mathbf{p})/dt=-\Gamma_{ij}(\mathbf{p})\frac{\delta(F/kT)}{\delta h_j(\mathbf{p})}+\zeta_i(\mathbf{p};t) \ , \tag{20}$$

where ζ is a stochastic noise term and $\Gamma_{ij}(\mathbf{p})$ are the dissipation constants. If the correlation time of the stochastic noise is much less than the correlation time for phason fluctuations $\tau_{\rm corr}$, we can treat its correlation function as proportional to a δ function. Then

$$\langle\zeta_i(\mathbf{p};t')\zeta_j(\mathbf{p};t'')\rangle\approx 2\Gamma_{ij}(\mathbf{p})\delta(t'-t'') \ . \tag{21}$$

It is well known that this relationship between noise correlations and dissipation constants must be satisfied if the steady-state fluctuations of the Langevin distribution are to agree with their equilibrium expectations given by Eq. (19). The noise does not vanish in the "hydrodynamic limit" $\mathbf{p}\to\mathbf{0}$, since the spatially averaged $\mathbf{h}$ changes with each Monte Carlo move. Furthermore, in a large system $\Gamma_{ij}(0)$ must have icosahedral symmetry, but the only such second-rank tensor is proportional to the Kronecker δ_{ij}. Thus we can replace $\Gamma_{ij}(\mathbf{p})\to\Gamma\delta_{ij}$ for small $\mathbf{p}$.

For wave vectors along the coordinate axes, $\mathbf{K}(\mathbf{p})$ is diagonal, and Eq. (20) reduces to

$$dh_i(\mathbf{p}_{i+k})/dt=-\frac{1}{\tau_{\rm corr}(k,p)}h_i(\mathbf{p}_{i+k})+\zeta_i(\mathbf{p}_{i+k};t) \ , \tag{22}$$

with

$$\tau_{\rm corr}(k,p)\equiv[\Gamma K_{ii}(\mathbf{p}_{i+k})]^{-1} \ . \tag{23}$$

The right-hand side of Eq. (23) has the same value for any $i=1,2,3$ due to the cyclic symmetry of Eq. (17). Using the sign-change symmetry of Eq. (17), the temporal correlation function $\langle h_i(\mathbf{p}_j)_0h_k^*(\mathbf{p}_l)_t\rangle$ can be nonzero only when $i=k$ and $\mathbf{p}_j=\mathbf{p}_l$. The relation

$$\langle h_i(\mathbf{p}_j)_0h_i^*(\mathbf{p}_j)_t\rangle=\langle h_{i+k}(\mathbf{p}_{j+k})_0h_{i+k}^*(\mathbf{p}_{j+k})_t\rangle \ , \tag{24}$$

a consequence of the cyclic permutation symmetry of Eq. (17), motivates the definition of the symmetry averaged time correlation function

$$C_{k,p}(t)=\tfrac{1}{3}\sum_{i=1}^{3}\langle h_i(\mathbf{p}_{i+k})_0h_i^*(\mathbf{p}_{i+k})_t\rangle \ . \tag{25}$$

With the assumption [Eq. (21)], the correlation function decays exponentially,

$$C_{k,p}(t)=C_{k,p}(0)e^{-t/\tau_{\rm corr}(k,p)} \ , \tag{26}$$

and Eq. (23) is in fact the correlation time. Since $\mathbf{K}(\mathbf{p})\sim|\mathbf{p}|^2$ at small $\mathbf{p}$, we see that Eq. (23) predicts the slowest mode in a finite system relaxes as L^z with $z=2$, as has been noted by Tang.[19]

3. *Projection images*

We now turn to the problem of interpreting simulated HRTEM images.[28–31] First consider the images we expect from projections along a five fold axis $\mathbf{e}_6^{\parallel}$ of *perfect* tilings in the limit of infinite slice thickness θ. Rhombohedron vertices which project onto the same spot have phason-space coordinates along a line l_6 parallel to $\mathbf{e}_6^{\parallel}$ [see Eqs. (4) and (5)]. The distribution of points in the acceptance domain is uniform and dense,[32] so the "brightness" of a spot is proportional to the length of l_6 within the acceptance domain. In fact, most l_6 lines which intersect the rhombic triacontahedral acceptance domain have a length on the order of the diameter of the domain since the acceptance domain is nearly spherical. Thus most spots are of comparable brightness.

The positions of spots in the two-dimensional projec-

tion images $\mathbf{s}^{\parallel}$ are specified by

$$\mathbf{s}^{\parallel}=\sum_{\alpha=1}^{5} n_\alpha \mathbf{f}_\alpha^{\parallel} ,$$

where the corresponding phason-space positions

$$\mathbf{s}^{\perp}=\sum_{\alpha=1}^{5} n_\alpha \mathbf{f}_\alpha^{\perp}$$

lie within a decagon with edge vectors $\mathbf{f}_\alpha^{\perp}$ (see Sec. II). The $\mathbf{f}_\alpha^{\parallel}(\mathbf{f}_\alpha^{\perp})$ are the five nonzero projections of $\mathbf{e}_\alpha^{\parallel}$ $(\mathbf{e}_\alpha^{\perp})$ onto the two-dimensional plane with normal vector $\mathbf{e}_6^{\parallel}$ $(\mathbf{e}_6^{\perp})$, while the projection of the rhombic triacontahedral acceptance domain along $\mathbf{e}_6^{\perp}$ produces the decagonal acceptance domain. A row of spots along the $\mathbf{f}_\beta^{\parallel}$ direction in the projection corresponds to vertices along a line m_β parallel to $\mathbf{f}_\beta^{\perp}$ inside the decagon. Due to variations of the lengths of projected lines l_6 along a given m_β, the brightness of spots along any row in the real space image will display short-wavelength variations.

Viewing the projection image obliquely along a symmetry direction, say $\mathbf{f}_5^{\parallel}$, essentially performs another projection down to a one-dimensional space, both in physical and in phason space. The four normalized one-dimensional physical and phason-space vectors $\mathbf{g}_\alpha=(g_\alpha^{\parallel},g_\alpha^{\perp})$, produced by projection along $\mathbf{f}_5^{\parallel}$ and $\mathbf{f}_5^{\perp}$ are

$$\begin{aligned}&\mathbf{g}_1=\eta(\tau,1),\quad \mathbf{g}_2=\eta(1,-\tau) ,\\ &\mathbf{g}_3=\eta(-\tau,-1),\quad \mathbf{g}_4=\eta(-1,\tau) ,\end{aligned} \tag{27}$$

and the 1D acceptance domain is an interval of length $2\eta\tau^2\cong 2.75$. The average brightness of a row is proportional to the area of the corresponding slice through the triacontahedral acceptance domain; this is a function of the 1D phason coordinate which goes to zero at the end points of the 1D acceptance domain. The sequence of row spacings may be considered as projections onto the physical space of square lattice points within a strip of width $\cong 2.75$ and slope τ as in Fig. 5(a). There are four physical space distances $\eta\tau$, η, $\eta\tau^{-1}$, and $\eta\tau^{-2}$ corresponding to displacements (0,1), (1,0), $(-1,1)$, and $(2,-1)$ on the square lattice.[33] Note that the smaller the physical space displacement between rows, the larger the phason-space displacement. Hence closely spaced rows of the projection image generally correspond in phason space to points near the borders of the strip, and tend to be dim and hard to see.

Upon randomization of the tiling, the short-wavelength phason fluctuations "soften" the boundary of the 3D acceptance domain of Eq. (8), i.e., the probability of including a point with a phason coordinate near the boundary no longer jumps from one to zero, but instead decays smoothly. The long-wavelength fluctuations in effect make a slowly varying shift of the center of mass of the acceptance domain without changing its shape. Brightness variations produced by short-wavelength phason fluctuations are camouflaged by the inherent brightness variations mentioned above. Long-wavelength phason fluctuations, on the other hand, produce noticeable defects in the projection image of a slice where one row dims as the brightness of an adjacent row increases.[29] The less bright rows, having a phason coordinate nearest the boundaries of the 1D acceptance domain, are the most sensitive to long-wavelength phason fluctuations which can move them in and out of the acceptance domain.

To produce a long-wavelength brightness fluctuation in a bright row, the column average of the coarse-grained phason coordinate

$$\mathbf{H}(x,y)\equiv\frac{1}{\theta}\int_{-\theta/2}^{\theta/2}\mathbf{h}(x,y,z)dz \tag{28}$$

must fluctuate by a distance of order the size of the acceptance domain, i.e., of order unity. By the inverse transform of Eq. (16),

$$\mathbf{H}(x,y)=\frac{1}{\sqrt{V}}\int\int\int\frac{\sin(p_z\theta/2)}{(p_z\theta/2)}e^{-i(p_x x+p_y y)}\mathbf{h}(\mathbf{p})dp_x dp_y dp_z , \tag{29}$$

and applying Eq. (19), the thickness dependence has the form

$$\langle|\mathbf{H}|^2\rangle\approx\theta_0/\theta , \tag{30}$$

where θ_0 is a parameter we will call the "crossover thickness" (it depends in part on short-wavelength properties, so we cannot evaluate it from the stiffness constants). The distribution of $\mathbf{H}$, like $\mathbf{h}$, is Gaussian, so the probability per unit area of a fluctuation of order unity, corresponding to a brightness fluctuation in a bright row, is expected to scale as[12]

$$\exp(-1/\langle|\mathbf{H}|^2\rangle)\sim\exp(-\theta/\theta_0) . \tag{31}$$

III. IMPLEMENTATION

The Monte Carlo runs are composed of initialization, equilibration, and measurement stages.

The initialization stage generates and stores the positions of vertices of the tiling, and their connectivity along rhombohedral edges. The initial configuration is a cubic unit cell of an approximant with $\bar{\tau}=F_n/F_{n-1}$. When F_n and F_{n-1} are both odd the initial periodic approximant has body-centered-cubic periodicity instead of simple-cubic periodicity.

The equilibration stage rearranges the tiling in a sequence of elementary moves, each of which repositions one vertex. "Movable" vertices are those vertices located inside a rhombic dodecahedron composed of two oblate and two prolate rhombohedra; this is true if and only if the vertex is connected along rhombohedron edges to exactly four other vertices. The repositioning of a vertex is equivalent to reflecting the rhombic dodecahedron in the midplane normal to the long symmetry axis. This is identical to the move used by Tang[19]; it is the natural generalization to three dimensions of the rearrangement of three

rhombi and one vertex forming a nonregular hexagon in rhombus tilings.[15] The number of tiles and vertices is clearly conserved, and we believe the rearrangement process is ergodic.[34]

To ensure that the steady-state weight of all configurations is equal, the Monte Carlo process satisfies detailed balance. Tang[19] implements detailed balance by randomly picking a vertex and when it is movable, repositioning it. In our simulation we randomly select one of the movable vertices and reposition the movable vertex. It can easily be checked that, in the steady state of this random process, the weights of configurations are not strictly equal but are proportional to number of movable vertices N_m. This is corrected by a weighting factor proportional to N_m^{-1}; since the fluctuations in N_m are $O(N^{1/2})$, the loss of efficiency is negligible in a large system. We correspondingly increase the elapsed-time variable t by an increment equal to N_m^{-1} of the starting configuration. [This time increment is equivalent to the average number of vertices (movable and nonmovable) that would be randomly chosen from the configuration before a movable vertex is found, divided by the number of tiles in the system.] The variable time increment ensures that on average, one unit of our time is equivalent to one Monte Carlo step per vertex in Tang's dynamics. Whereas 24% of the vertices in the initial or "perfect" tiling are movable,[35] in the fully equilibrated random tiling approximately 18% of the vertices are movable.

The measurement stage monitors the positions of the tile vertices and either measures the magnitude of the fluctuations or projects a section of the tiling onto a plane to create an image. Within a run, phason-fluctuation measurements are separated by time intervals approximately equal to the correlation time $\tau_{\rm corr}$. To ensure statistical independence, each run is separated by at least $3\tau_{\rm corr}$ from the preceding run and the initialization of the system. Because of the quadratic size dependence $\tau_{\rm corr}\sim L^2$ (see below), in the larger systems it is most efficient to update the vertex connectivity information after each Monte Carlo move while only calculating the vertex positions during measurement states. The momentum space phason fluctuations are calculated by the summation over vertex positions

$$\bar{\mathbf{h}}(\mathbf{p})=\frac{\sqrt{V}}{N}\sum_{\mathbf{r}}\bar{\mathbf{h}}(\mathbf{r})e^{i\mathbf{p}\cdot\mathbf{r}}\ , \tag{32}$$

which reduces to Eq. (16) in the continuum limit. Although phason-fluctuation measurements use the commensurate projection coordinates $\bar{\mathbf{h}}$, for notational simplicity we henceforth omit the overbar.

To produce images we first project the tile vertices onto a two-dimensional plane: $\mathbf{r}\rightarrow(x',y')$. The coordinates $\mathbf{r}'=(x',y',z')$ are related to the physical space coordinates $\mathbf{r}=(x,y,z)$ by the rotation $\mathbf{r}'=\underline{\mathbf{M}}\mathbf{r}$. [We consider (x,y,z) as extended by periodic boundary conditions.] When the projection is along a twofold symmetry axis, $\underline{\mathbf{M}}$ is simply the identity matrix. When the projection is along a fivefold symmetry axis

$$\underline{\mathbf{M}}=\begin{bmatrix}1 & 0 & 0\\ 0 & \tau/\eta & -1/\eta\\ 0 & 1/\eta & \tau/\eta\end{bmatrix}\ . \tag{33}$$

The projected vertices lie within the bounds

$$\tfrac{1}{2}(L-\theta)<z'<\tfrac{1}{2}(L+\theta)\ , \tag{34}$$

where θ is the thickness of the slice. The area shown in our figures was chosen to be

$$0<x'<L,\quad 0<y'<L\ .$$

Our primary interest here is in how the apparent disorder is affected by slice thickness. Therefore, rather than attempting a realistic decoration or allowing for dynamical (multiple scattering) effects, we have generated schematic HRTEM's by decorating tiles in the simplest possible manner. To each vertex in our slice we assign an "atom" with an "electron" density $\rho(\mathbf{r})$ of the form

$$\rho(\mathbf{r})=\exp\left[-\left[\frac{|\mathbf{r}|}{a}\right]^2\right]\ , \tag{35}$$

where a is the "atomic radius" (taken to be 0.3 rhombohedron edge lengths). Thus, the projected density is

$$\rho_{\rm 2D}(x',y')\equiv\sum_{\{i:\ |z'_i-L|<\theta/2\}}\rho(x'-x'_i,y'-y'_i)\ .$$

To efficiently calculate the electron density at each raster point, we binned the vertices according to their projected positions into boxes of linear dimension $3a$. Only those vertices within the bin containing the raster point, and the vertices in the eight surrounding bins are used in determining the electron density. The projected electron density is represented in the images by shades of gray using a linear scale, with lighter regions corresponding to *higher* electron densities. The range of values of the pro-

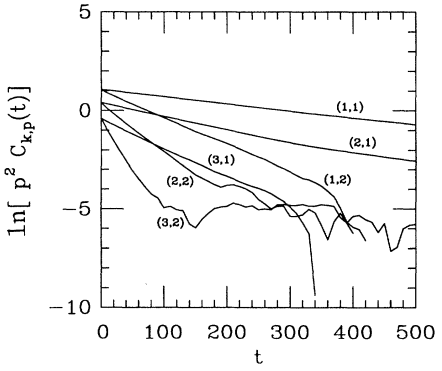

FIG. 1. Plots of $\ln[p^2C_{k,p}(t)]$ vs time t for a system of 10 336 tiles. Plots are labeled by (k,n) where $p=(2\pi/L)n$. The correlation times $\tau_{\rm corr}(k,p)$, as determined by the inverse magnitude of the slopes are $\tau_{\rm corr}(1,2\pi/L)\cong 280$, $\tau_{\rm corr}(2,2\pi/L)\cong 145$, $\tau_{\rm corr}(3,2\pi/L)\cong 63$, $\tau_{\rm corr}(1,4\pi/L)\cong 70$, $\tau_{\rm corr}(2,4\pi/L)\cong 38$, and $\tau_{\rm corr}(3,4\pi/L)\cong 17$.

jected electron density (needed to normalize the gray density scale) was determined by sampling the electron densities of one-thirtieth of the raster points.

IV. RESULTS AND DISCUSSION

A. Stiffness constants and dynamics

In calculating the stiffness constants and correlation functions, Fourier-transformed phason fluctuations $\mathbf{h}(\mathbf{p})$ are monitored for wave vectors of magnitude $|\mathbf{p}|=p=2n\pi/L$ $(n=1,2)$ along the coordinate axes $(\mathbf{p}=\mathbf{p}_j,\ j=x,y,z)$. Figure 1 plots $\ln[p^2 C_{k,p}(t)]$, where $C_{k,p}(t)$ is the correlation function, versus time t for a system of 10 336 tiles. The basically linear behavior of the curves, indicating an exponential decay of correlations, is consistent with Eq. (26), and the inverse of the magnitude of the slopes gives the correlation time $\tau_{\rm corr}$. The k,p dependence of $\tau_{\rm corr}$ (as listed in the caption of Fig. 1) is consistent with Eqs. (17) and (23), and we infer the kinetic coefficient Γ is roughly 0.096.[36] The largest correlation time $\tau_{\rm corr}$ for a system of linear dimension L,

$$\tau_{\rm corr}=\tau_{\rm corr}\left[k,\frac{2\pi}{L}\right]\propto L^2\ , \tag{36}$$

is the time scale that must be considered in the equilibration of Monte Carlo runs.

In accordance with Eqs. (19) and (17), the stiffness constants K_1 and K_2 are determined by a least-squares fit to the equations

$$\underline{\mathbf{B}}\,\underline{\mathbf{K}}=\underline{\mathbf{H}}+\delta\underline{\mathbf{H}}\ , \tag{37}$$

where

$$\underline{\mathbf{B}}=\begin{bmatrix}1 & -\frac{1}{3}\\ 1 & \tau-\frac{1}{3}\\ 1 & 1-\frac{1}{3}-\tau\end{bmatrix}\ ,\quad \underline{\mathbf{H}}=\frac{1}{p^2}\begin{bmatrix}C_{0,p}(0)^{-1}\\ C_{-1,p}(0)^{-1}\\ C_{1,p}(0)^{-1}\end{bmatrix}\ ,$$
$$\underline{\mathbf{K}}=\begin{bmatrix}K_1\\ K_2\end{bmatrix}\ , \tag{38}$$

and $\delta\underline{\mathbf{H}}$ represents the random and systematic errors associated with $\underline{\mathbf{H}}$. Figure 2 plots the stiffness constants versus the inverse system size $1/L$. The upper data points represent K_1 for wave vectors of magnitude $2\pi/L$ (solid) and $4\pi/L$ (dot-dashed) and the lower data points represent K_2 for wave vectors of magnitude $2\pi/L$ (dotted) and $4\pi/L$ (dashed). The zigzag pattern of the data points with increasing system size is a result of the sign alternation of E_n with n as shown in Eq. (13). Extrapolation of the data to the $L=\infty$ limit provides the estimates

$$K_1=0.81\pm0.01\ \text{ and }\ K_2=0.495\pm0.01\ . \tag{39}$$

The coincidence of the ratio K_1/K_2 with τ is intriguing.

Tang[19] has already measured the elastic constants by a different approach. As might be done in a real experiment, he measures the inverse-square wings of diffuse scattering around Bragg peaks and fits them to the predictions of Jarić and Nelson.[11] Tang's values, when adapted to the conventions of Eqs. (15) and (16) [his conventions differ by factors of $(2\pi)^3$ and N/V], give $K_1=0.92$ and $K_2=0.57$, with an accuracy of about 10%, consistent with our results. Our errors are smaller because our method for extracting stiffnesses is more direct and because we use time-averaged, rather than instantaneous information.

To determine the magnitude of the inconsistency in the

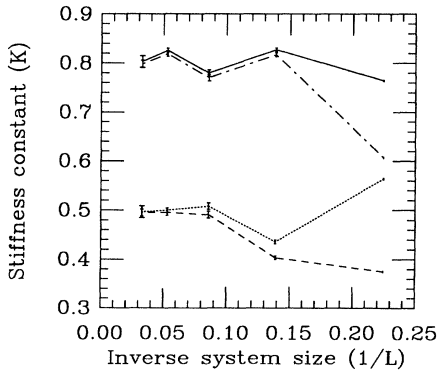

FIG. 2. The stiffness constants vs inverse system size $(1/L)$. The upper data points represent K_1 for wave vectors of magnitude $2\pi/L$ (solid) and $4\pi/L$ (dotted-dashed) and the lower data points represent K_2 for wave vectors of magnitude $2\pi/L$ (dotted) and $4\pi/l$ (dashed). From extrapolation to the $L=\infty$ limit we estimate $K_1=0.81\pm0.01$ and $K_2=0.495\pm0.01$.

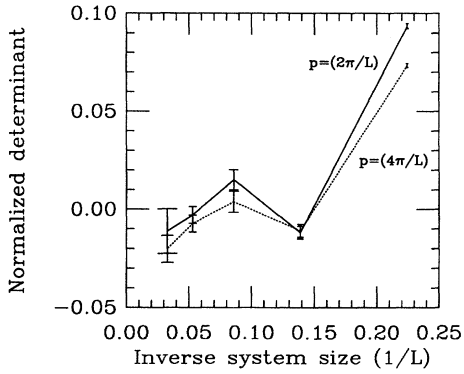

FIG. 3. The normalized determinant D decreases in magnitude with increasing inverse system size $(1/L)$ indicating decreasing finite-size effects.

equations $\underline{B}\,\underline{K}=\underline{H}$, we define the normalized determinant

$$D=\frac{\det[\underline{B}|\underline{H}]}{\sqrt{8}|\underline{H}|}\ , \tag{40}$$

where the denominator is the product of the two-norm of the columns of $\underline{B}$ and $\underline{H}$, and $[\underline{B}|\underline{H}]$ is the 3×3 concatenation of $\underline{B}$ and $\underline{H}$. D provides an independent means of estimating the magnitude of the finite-size effects. Figure 3 plots D versus inverse system size $(1/L)$ for wave vectors of magnitude $2\pi/L$ (solid) and $4\pi/L$ (dotted). As expected, the sign of D appears to alternate, and the magnitude of D decreases to zero, with increasing system size confirming the vanishing of finite-size effects.

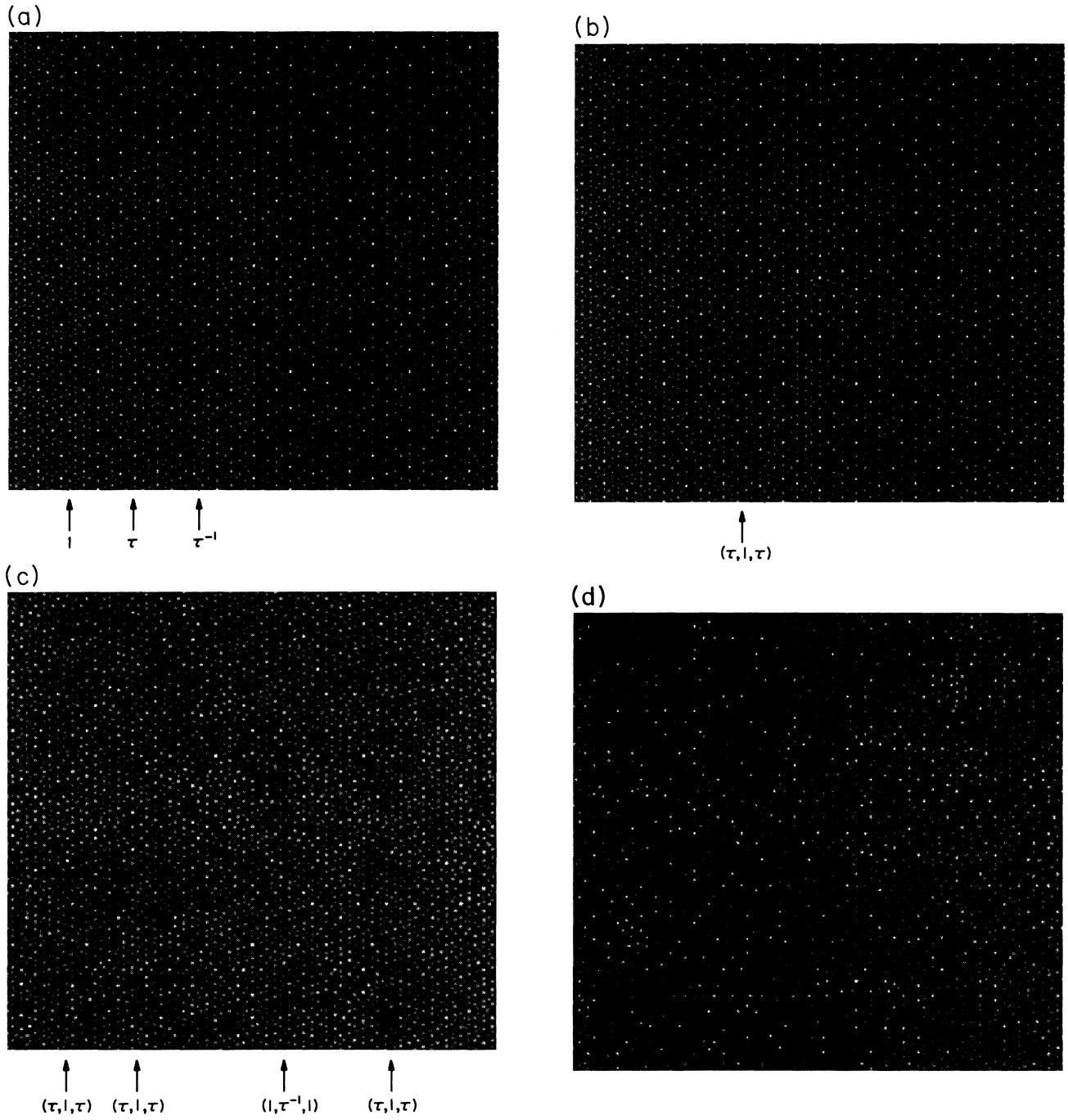

FIG. 4. Projections of slices of thickness θ of a random tiling along a fivefold symmetry axis. The area shown is $48.4a_R\times48.4a_R$, where a_R is the rhombohedron edge length. The atomic radius a is $0.3a_R$. Large "electron" densities correspond to white regions. (a) $t=0$, $\theta=25a_R$. (b) $t=4800$, $\theta=25a_R$. (c) $T=4800$, $\theta=15a_R$. (d) $t=4800$, $\theta=5a_R$. Arrows in (a) mark and label row spacings. Arrows in (b)–(d) mark and label defects.

B. Simulated lattice images

Figures 4(a)–4(d) show projections of slices of the $\bar{\tau}=21/13$ tiling containing 185 472 vertices. The square area shown has linear dimension slightly smaller than that of the simulation cell. Figure 4(a) shows a projection along a fivefold axis at $t=0$ of a slice with thickness 25. Figure 4(b) shows the same projection at $t=4800\approx 3\tau_{\rm corr}$. The main difference between Figs. 4(a) and 4(b) comes from small groups of weak spots that appear blurred into a single large spot. These clusters of spots lie in several closely spaced rows and so are most affected by long-wavelength phason fluctuations on randomization of the tiling.

By obliquely sighting along symmetry directions of Fig. 4(b) one can see rows of spots spaced essentially as in Fig. 4(a)—a quasiperiodic sequence as described in Sec. II A 3. We require three labels for the types of spacings between rows [examples are marked in Fig. 4(a)]: (i) rows separated by a dark band are said to be separated by a τ spacing, (ii) closely spaced (yet distinct) rows have a unit spacing, (iii) pairs of rows that appear to have almost merged, are said to be separated by a τ^{-1} spacing. The τ^{-1} spacings generally occur for a pair of dim rows between a pair of bright rows as a $\{1,\tau^{-1},1\}$ sequence. Although smaller τ^{-2} spacings also occur, they are difficult to see and the following analysis neglects their existence. The sequence of row separations extracted by an oblique viewing of Fig. 4(b) with the page held in the normal reading orientation is, from left to right, $\{1,\tau^{-1},1,\tau,1,\tau,1,\tau^{-1},1,\tau,1,\tau,\tau,1,\ldots\}$.

We confirm the quasiperiodicity of the row positions by "lifting" the sequence to a path connecting points on the square lattice as in Fig. 5(b). The row separations termed τ, 1, and τ^{-1} are mapped to displacements along the physical space axis $g^{\parallel}=\eta(\tau,1)$ of length $\eta\tau$, η, and $\eta\tau^{-1}$, which in turn correspond to (0,1), (1,0), and $(-1,1)$ displacements in the square lattice, respectively. The path lies within the strip of width $\cong 2.75$ and slope τ delimited by the dotted lines, confirming the quasiperiodicity of the sequence (see Sec. II A 3). Within the strip, there are a number of points near the boundaries that are not on the path in Fig. 5(b) since (i) we have not attempted to observe the τ^{-2} spacings and (ii) defects obscure one row in a pair of closely spaced rows (see below). On lifting the row separations of a perfect tiling [e.g., Fig. 4(a)] to a path on the square lattice all the lattice points within a strip of width $\cong 2.75$ would be represented.

A comparison of Figs. 4(a) and 4(b) show how the randomization of the tiling decreases the uniformity of brightness along rows of spots. Row "defects" occur when the brightness of one row vanishes as an adjacent row appears, giving the appearance of a single jagged row with an ill-defined position. For instance, what we call a $\{1,\tau^{-1},1\}$ defect (labeled according to the row spacing environment in the absence of brightness variations) appears in different intervals down the length of the row as a $\{1+\tau^{-1},1\}=\{\tau,1\}$ or as a $\{\tau,1\}$ sequence. Arrows in Figs. 4(b)–4(d) mark and label defects.

Comparison of Figs. 4(b)–4(d) shows an increasing frequency of defects with decreasing slice thickness, as predicted by Eq. (30). For instance: the slice of thickness 5 has defects in almost every row; there are a number of $\{\tau,1,\tau\}$ defects in the slice of thickness 15; and there are only a few "weak defects," (i.e., the brightness of a defective row dims but does not vanish) in $\{\tau,1,\tau\}$ sequences in the slice of thickness 25. We note that defects in dim rows (usually in $\{1,\tau^{-1},1\}$ sequences) are still common in slices of thickness 25. Recalling that the crossover thickness θ_0 is determined by the slice thickness at which defects in *bright* rows become infrequent, we conclude that θ_0 is approximately 15 rhombohedral edge lengths.

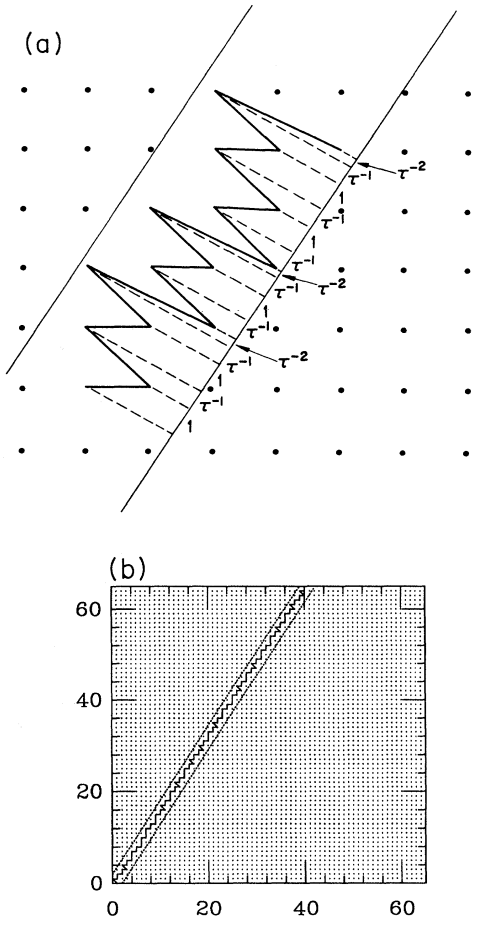

FIG. 5. (a) Projected positions of lattice points within the strip of width $\cong 2.75$ correspond to a sequence of row spacings from the projected image of an infinite perfect tiling. (b) Projections of line segments along the connected path on the square lattice onto $g^{\parallel}$ correspond to the sequence of spacings between rows of spots in Fig. 4(b). The limited transverse deviation of the path from a line of slope τ indicates that the sequence is quasiperiodic.

Although a rough description of the atomic structures of *i*(Al-Mn-Si) (Ref. 23) and *i*(Al-Cu-Fe) (Refs. 12, 37, and 1) in terms of rhombohedral tiles of edge length $a_R\approx 0.460$ and 0.446 nm, respectively, has been noticed, we do not believe the structure is free to rearrange as a

random tiling at the 0.5-nm scale. A more plausible model is that the random degrees of freedom are at the scale of clusters of 50 or more atoms. In the canonical cell model the (nonrhombohedral) tiles have edge lengths of 0.9 or 1.3 nm, with clusters at the vertices.[38] In another model[39] the degrees of freedom are Ammann rhombohedra of edge length $a_R \approx \tau^2 0.45$ mn$\cong 1.2$ nm, and again there are clusters of atoms at the vertices.

Motivated by these models where the tile vertices represent clusters of atoms, we computed lattice images from the same random-tiling configurations in a second way. A primary structural unit of the *i*(Al-Mn-Si) phase

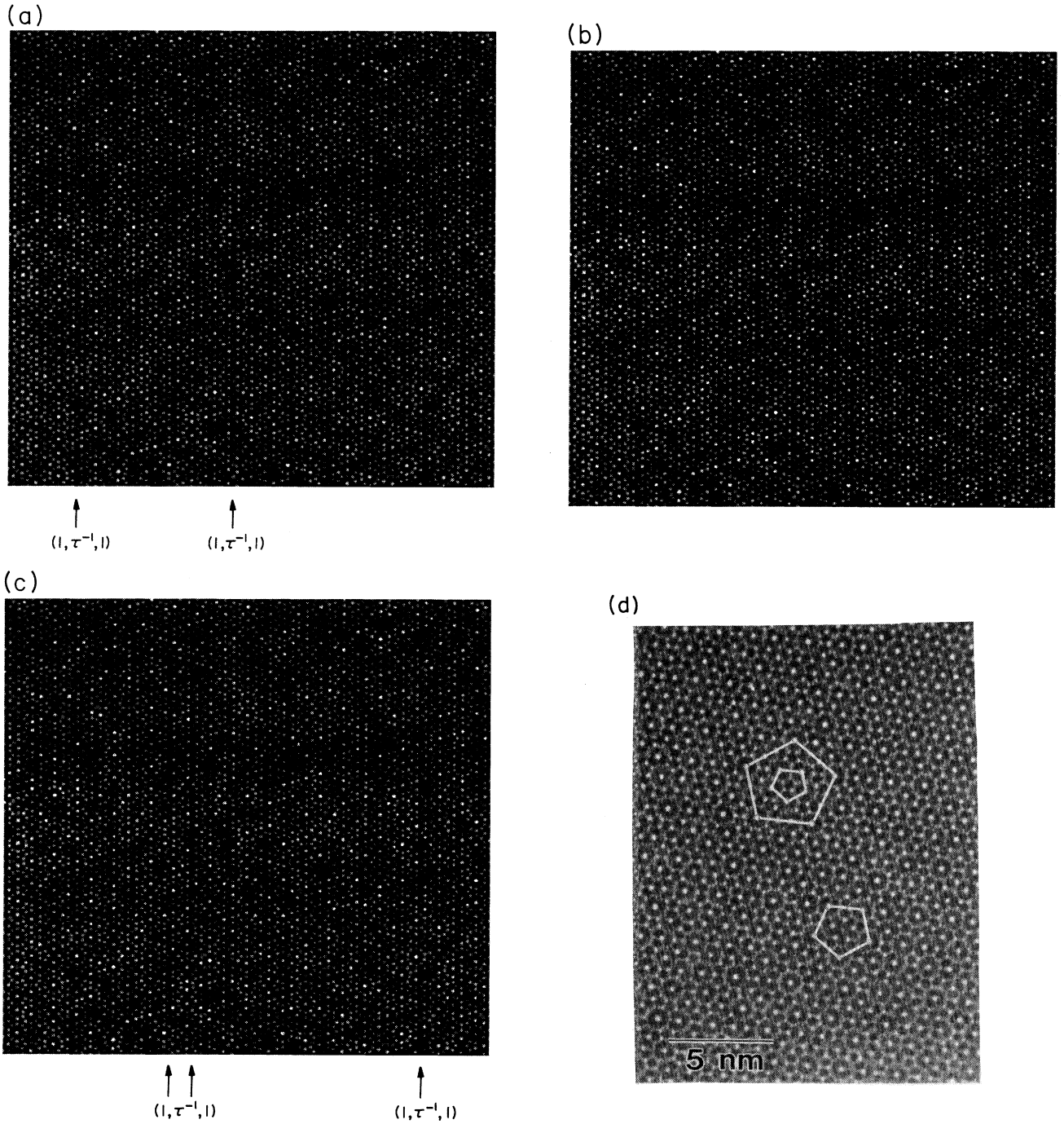

FIG. 6. Projections of expanded/decorated slices of thickness θ of a random tiling along a fivefold symmetry axis at time $t=4800$. The area shown is $48.4a_R \times 48.4a_R$, where a_R is the rhombohedron edge length. The atomic radius a is $0.3a_R$. Large "electron" densities correspond to white regions. Defects in $\{\tau,1,\tau\}$ sequences are marked with arrows. (a) $\theta=65a_R$. (b) $\theta=25a_R$. (c) $\theta=15a_R$. (d) is an actual HRTEM of an Al-Cu-Fe alloy along a fivefold symmetry axis [reproduced from Figure 3 of Hiraga *et al.* (Ref. 14), with permission of the authors]; the slice thickness is unknown.

is the Mackay icosahedron,[23] a cluster of 54 atoms in which 12 strongly scattering Mn atoms form an icosahedron around the cluster center. Accordingly, as a crude approximation to the structure of actual quasicrystalline materials, we expand the tiling rhombohedra by a factor of τ^2 and replace each vertex by an icosahedron of 12 atoms, each atom at unit distance from the vertex along the icosahedral basis directions. Accordingly, the new atomic positions $\mathbf{r}'_{i\alpha}$ are related to the old vertex positions $\mathbf{r}_i$ by

$$\mathbf{r}'_{i\alpha} \equiv \tau^2 \mathbf{r}_i \pm \mathbf{e}^{\parallel}_{\alpha} .$$

The expansion/decoration process is closely related to the inflation process for generating perfect Penrose tilings. The inflation in physical space by a factor of τ^2 corresponds to a deflation in phason space by the same factor, reducing the magnitude of the phason fluctuations, and therefore reducing the row defects. Scaling $\mathbf{H}$ by τ^{-2}, and θ by τ^2 in Eq. (30) we see that the expansion/decoration process reduces the crossover thickness of Eq. (31) by a factor of τ^2. Therefore we expect the crossover thickness for the expanded/decorated tiling to be approximately $15/\tau^2 \cong 6$ units, corresponding to a distance of about 3 nm.

The expanded/decorated images of Figs. 6(a)–6(c) appear very similar to the undecorated images of Fig. 4. Although the expanded/decorated slices have a more mottled appearance than unexpanded slices of the same thickness [compare Figs. 4(c) and 6(c)], an oblique view of both figures shows that the expanded/decorated image has substantially fewer bright-row defects; adjacent bright rows in the expanded/decorated tiling grow brighter or dimmer *together*. On the other hand, defects in dim rows occur even in thick slices [such defects are marked in Fig. 6(a)]. Short-wavelength brightness fluctuations are quite noticeable in the thinner slices. The expanded/decorated slices cannot be used to determine the crossover thickness since, as the slice thickness approaches the expected crossover thickness of 6 rhombohedral edge lengths, short-wavelength brightness fluctuations obscure row defects.

An actual HRTEM[14] of a conventionally solidified Al-Cu-Fe alloy is displayed in Fig. 6(d). The qualitative features of the HRTEM are consistent with those of the decorated and undecorated simulation images: regular decagons and pentagons appear with size ratios that are multiples of τ, and quasiperiodically spaced rows of bright and dim spots appear upon oblique viewing. On the premise that the tiling rhombohedra have an edge length a_R of 1.2 nm, the second smallest size regular decagon in the expanded/decorated tiling images with vertex to vertex diameter $(4/\tau\sqrt{5})a_R \approx 1.1 a_R$ are to be compared to the smallest regular decagons in the HRTEM with a diameter of $\cong 1.3$ nm. Although the exposure makes it difficult to see the weaker $\{1,\tau^{-1},1\}$ sequences, it appears that defects in these sequences do occur. There are no defects in bright rows separated by a $\{\tau,1,\tau\}$ sequence, indicating that the thickness of the HRTEM slice is greater than the crossover thickness.

C. Conclusions

In conclusion, our simulation results (i) demonstrate that projections of slices of equilibrated, expanded/decorated tilings as thin as 6 rhombohedral edge lengths display the qualitative features of HRTEM images, (ii) accurately determine the values of the two phason-stiffness constants, and (iii) confirm the Langevin description of the coarse-grained phason dynamics.

The analytic argument given in Sec. II D is valid quite generally and shows that phason fluctuations become invisible in HRTEM images from any sufficiently thick specimen. A realistic and complete model of a random-tiling structure would allow the prediction of the crossover thickness sufficient to wash out fluctuations. Our images are only meant to be rough approximations to experimental images. There may not be a direct correspondence between the rhombohedral random-tiling model and a realistic random-tiling geometry for *i*(Al-Cu-Fe). Certainly the electron densities and the projection algorithm we used are crude approximations to the actual electron densities and dynamical (multiple diffraction) imaging effects. Nevertheless, we have sufficient faith in the crossover thickness deduced from our images with the icosahedron decoration that we propose its use in guiding future experiments.

We predict that there are essentially no defects in bright rows for samples thicker than 6 nm. This is less than the thinnest slices used in HRTEM studies. The experimental implications of our results are (1) any experimental observations aimed at revealing the degree of tiling disorder *must* include a determination of the thickness, (2) attempts should be made to study very thin specimens in order to see the disorder, and (3) attention should be paid to the exposure conditions. More disorder should be visible in the weaker rows of spots; consequently attempts should be made to resolve weak rows between the strong rows. The temptation to choose those focus and exposure conditions which lead to the most regular looking images may discard important information.

ACKNOWLEDGMENTS

L.J.S. was supported by the National Science Foundation through the Cornell Materials Science Center (MSC). V.E. was supported by the MSC, the Alfred P. Sloan Foundation, AT&T, the David and Lucile Packard Foundation, and the National Science Foundation Grant No. DMR-8958510. C.L.H. was supported by the Department of Energy Grant No. DE-FG02-89-ER45405. L.J.S. would like to thank the personable and helpful Materials Science Center computing staff and Peter Fraenkel for assistance with the optimization of the computer code.

[1]A. Tsai, A. Inoue, and T. Masumoto, Jpn. J. Appl. Phys. **26**, L1505 (1987).
[2]C. A. Guryan, A. I. Goldman, P. W. Stephens, K. Hiraga, A. Tsai, A. Inoue, and T. Masumoto, Phys. Rev. Lett. **62**, 2409 (1980).
[3]P. A. Bancel, Phys. Rev. Lett. **63**, 2741 (1989).
[4]D. Levine and P. J. Steinhardt, Phys. Rev. Lett. **53**, 2477 (1984).
[5]G. Y. Onoda, P. J. Steinhardt, D. P. DiVincenzo, and J. E. S. Socolar, Phys. Rev. Lett. **60**, 2653 (1988).
[6]J. E. S. Socolar, in *Quasicrystals,* edited by M. V. Jarić and S. Lundquist (World Scientific, Singapore, in press).
[7]V. Elser, Phys. Rev. Lett. **54**, 1730 (1985).
[8]C. L. Henley, Comments Condens. Mater. Phys. **13**, 59 (1987).
[9]M. Widom, in *Quasicrystals* (Ref. 6).
[10]T. C. Lubensky, S. Ramaswamy, and J. Toner, Phys. Rev. B **32**, 7444 (1985).
[11]M. V. Jarić and D. R. Nelson, Phys. Rev. B **37**, 4458 (1988).
[12]C. L. Henley, in *Quasicrystals and Incommensurate Structures in Condensed Matter,* edited by M. J. Yacamán, D. Romeu, V. Castaño, and A. Gómez (World Scientific, Singapore, in press).
[13]M. Audier and P. Guyot, in *Quasicrystals and Incommensurate Structures in Condensed* Matter (Ref. 12); M. Audier, P. Guyot, and Y. Brechet, Philos. Mag. Lett. **61**, 55 (1990).
[14]K. Hiraga, B.-P. Zhang, M. Hiragayashi, A. Inoue, and T. Masumoto, Jpn. J. Appl. Phys. **27**, L951 (1988).
[15]K. J. Strandburg, L. Tang, and M. V. Jarić, Phys. Rev. Lett. **63**, 314 (1989); K. J. Strandburg, Phys. Rev. B **40**, 6071 (1989).
[16]M. Widom, K. J. Strandburg, and R. H. Swendsen, Phys. Rev. Lett. **58**, 706 (1987).
[17]M. Widom, D. P. Deng, and C. L. Henley, Phys. Rev. Lett. **63**, 310 (1989).
[18]L. J. Shaw and C. L. Henley, unpublished; see Chap. 3 of L. J. Shaw, Ph.D. thesis, Cornell University, 1990.
[19]L.-H. Tang, Phys. Rev. Lett. **64**, 2390 (1990).
[20]K. J. Strandburg (personal communication).
[21]V. Elser, Acta Crystallogr. **A42**, 36 (1986).
[22]M. Duneau and A. Katz, Phys. Rev. Lett. **54**, 2688 (1985).
[23]V. Elser and C. L. Henley, Phys. Rev. Lett. **55**, 2883 (1985).
[24]V. Elser, in *XVth International Colloquium on Group Theoretical Methods in Physics,* edited by R. Gilmore (World Scientific, Singapore, 1987).
[25]C. L. Henley, J. Phys. A **21**, 1649 (1988).
[26]M. V. Jarić, in *XVth International Colloquium on Group Theoretical Methods in Physics* (Ref. 24).
[27]T. C. Lubensky, in *Aperiodic Crystals I,* edited by M. V. Jarić (Academic, New York, 1989).
[28]P. J. Steinhardt, Phys. Rev. Lett. **57**, 2769 (1986).
[29]P. W. Stephens and A. I. Goldman, Phys. Rev. Lett. **57**, 2770 (1986).
[30]K. Hiraga, M. Hirabayashi, A. Inoue, and T. Masumoto, Sci. Rep. Inst. Tohoku Univ. A **32**, 309 (1985).
[31]V. Elser, in *Aperiodic Crystals III: Extended Icosahedral Strucutres,* edited by M. V. Jarić and D. Gratias (Academic, New York, 1989).
[32]V. Elser, Phys. Rev. B **32**, 4892 (1985).
[33]This is closely related to the Fibonacci sequence which is generated from the projection of square lattice points within a strip of width $\eta\tau^2$ and slope τ. The two types of lengths in the sequence have a ratio of $1{:}\tau$.
[34]L.-H. Tang (personal communication) has outlined a proof, using dual-grid language, that every tiling can be reached by this move.
[35]C. L. Henley, Phys. Rev. B **34**, 797 (1986).
[36]A crude estimate of the magnitude of random noise at $\mathbf{p}=\mathbf{0}$, and hence of the coefficient Γ, is obtained by noting that each repositioning of a vertex i changes $\mathbf{r}_i^{\perp}$ by $u^{\perp}=2\tau^2\eta$ in one of the 30 icosahedral twofold symmetry directions. If we assume the successive changes are completely uncorrelated, then using Eq. (32) and the definition of time with movable fraction 0.18, we get $\Gamma=\frac{1}{6}(V/N)(u^{\perp})^2(0.18)\approx 0.15$. This is an overestimation of Γ since the random walk is in fact somewhat anticorrelated, e.g., a single isolated movable vertex can only move back and forth and so cannot contribute.
[37]C. L. Henley, in *Quasicrystals,* edited by T. Fujiwara and T. Ogawa (Springer, New York, in press).
[38]C. L. Henley, Phys. Rev. B **42**, 993 (1990).
[39]M. Audier and P. Guyot, Philos. Mag. B **53**, L43 (1986).

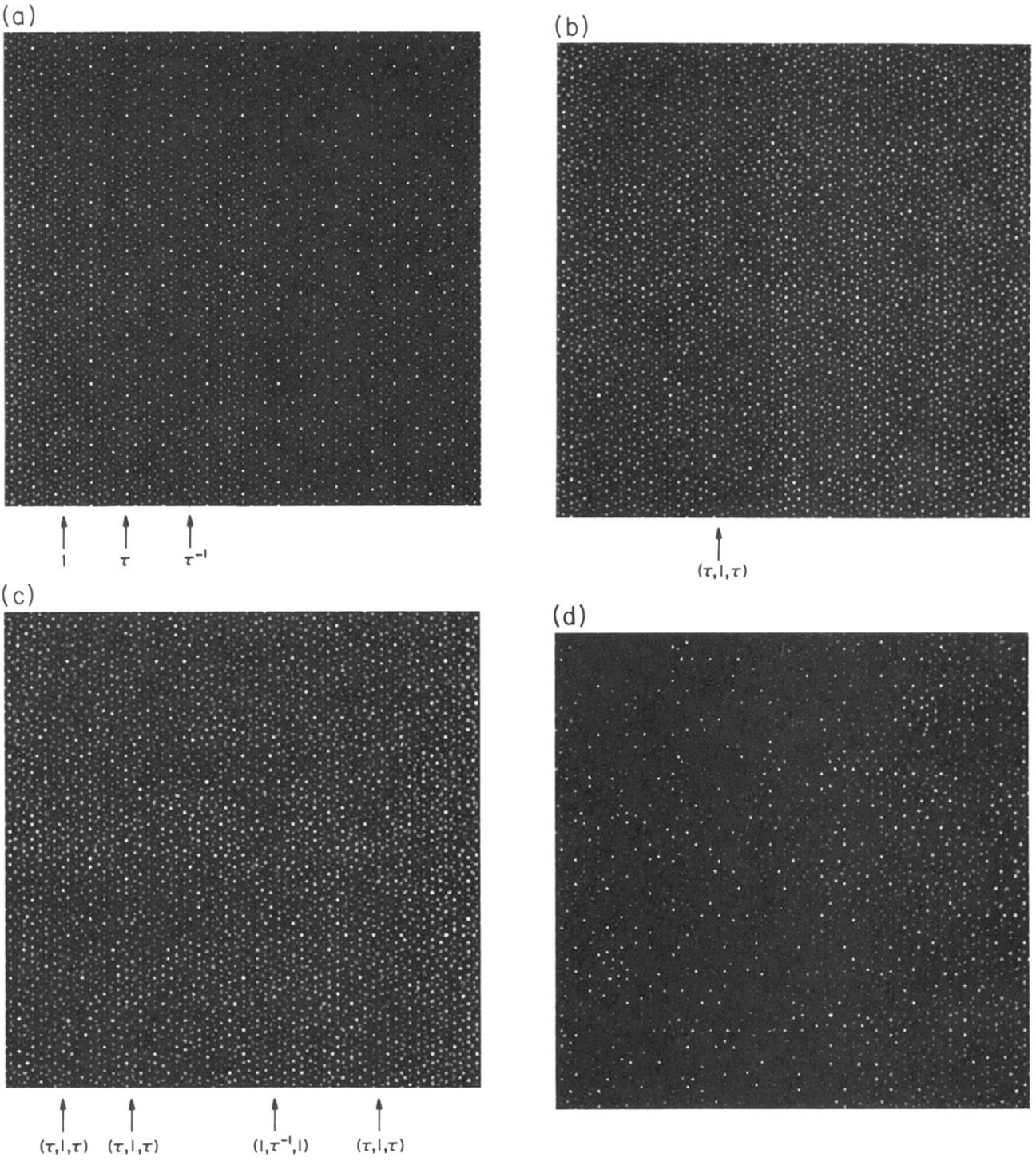

FIG. 4. Projections of slices of thickness θ of a random tiling along a fivefold symmetry axis. The area shown is $48.4a_R \times 48.4a_R$, where a_R is the rhombohedron edge length. The atomic radius a is $0.3a_R$. Large "electron" densities correspond to white regions. (a) $t=0$, $\theta=25a_R$. (b) $t=4800$, $\theta=25a_R$. (c) $T=4800$, $\theta=15a_R$. (d) $t=4800$, $\theta=5a_R$. Arrows in (a) mark and label row spacings. Arrows in (b)–(d) mark and label defects.

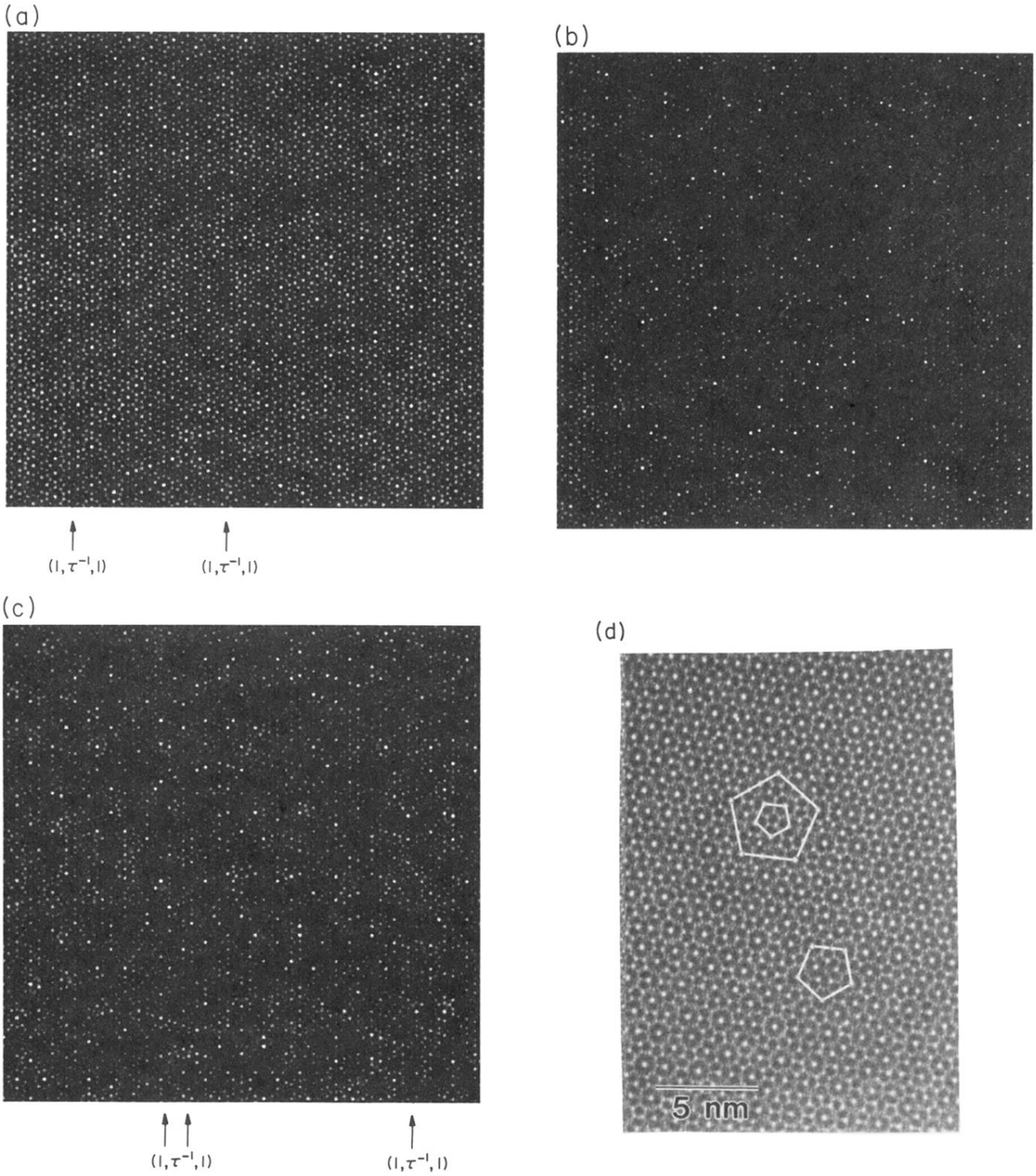

FIG. 6. Projections of expanded/decorated slices of thickness θ of a random tiling along a fivefold symmetry axis at time $t=4800$. The area shown is $48.4a_R \times 48.4a_R$, where a_R is the rhombohedron edge length. The atomic radius a is $0.3a_R$. Large "electron" densities correspond to white regions. Defects in $\{\tau,1,\tau\}$ sequences are marked with arrows. (a) $\theta=65a_R$. (b) $\theta=25a_R$. (c) $\theta=15a_R$. (d) is an actual HRTEM of an Al-Cu-Fe alloy along a fivefold symmetry axis [reproduced from Figure 3 of Hiraga *et al.* (Ref. 14), with permission of the authors]; the slice thickness is unknown.